# A novel semi-resolved CFD-DEM method with two-grid mapping

Che, Hanqiao; Windows-yule, Kit; O'sullivan, Catherine; Seville, Jonathan

*DOI:*
10.1002/aic.18321



*Document Version*
Publisher's PDF, also known as Version of record

*Citation for published version (Harvard):*
Che, H, Windows-yule, K, O'sullivan, C & Seville, J 2023, 'A novel semi-resolved CFD-DEM method with two-grid mapping: Methodology and verification', *AIChE Journal*. https://doi.org/10.1002/aic.18321

Received: 9 July 2023 | Revised: 7 October 2023 | Accepted: 12 November 2023

DOI: 10.1002/aic.18321

AIChE JOURNAL

RESEARCH ARTICLE

Particle Technology and Fluidization

# A novel semi-resolved CFD-DEM method with two-grid mapping: Methodology and verification

Hanqiao Che [1] | Kit Windows-Yule [1] | Catherine O'Sullivan [2] | Jonathan Seville [1]

[1]School of Chemical Engineering, University of Birmingham, Birmingham, UK

[2]Department of Civil and Environmental Engineering, Imperial College London, London, UK

**Correspondence**
Hanqiao Che, School of Chemical Engineering, University of Birmingham, Birmingham B15 2TT, UK.
Email: chehanqiao@outlook.com; h.che@bham.ac.uk

**Funding information**
EPSRC, Grant/Award Number: EP/P010393/1; EPSRC New Investigator Award, Grant/Award Number: EP/T034327/1

## Abstract

The semi-resolved Computational Fluid Dynamics coupled with the Discrete Element Method (CFD-DEM) method has emerged as approach to modeling particle-fluid interactions in granular materials with high particle size ratios. However, challenges arise from conflicting requirements regarding the CFD grid size, which must adequately resolve fluid flow in the pore space while maintaining a physically meaningful porosity field. This study addresses these challenges by introducing a two-grid mapping approach. Initially, the porosity field associated with fine particles is estimated using a coarse CFD grid, which is then mapped to a dynamically refined grid. To ensure conservation of total solid volume, a volume compensation procedure is implemented. The proposed method has been rigorously verified using benchmark cases, showing its high computational efficiency and accurate handling of complex porosity calculations near the surface of coarse particles. Moreover, the previously unreported impact of the empirical drag correlation on fluid-particle force calculations for both coarse and fine particles has been revealed.

**KEYWORDS**
bimodal particles, CFD-DEM, semi-resolved, two-grid method

## 1 | INTRODUCTION

Fluid-particle flows are common in various industrial sectors, and gaining insight into their behavior is crucial for developing new downstream processes and formulations,[1,2] as well as optimizing existing ones. Additionally, comprehending the coupled response of fluid-particle systems is vital in geomechanics applications, particularly in cases such as internal erosion,[3,4] where the overall system deformation may be relatively small. Computational Fluid Dynamics coupled with the Discrete Element Method (CFD-DEM) is a numerical approach that can simulate two-phase fluid-particle systems. It is a Lagrangian-Eulerian approach,[5,6] in which the fluid is modeled as a continuum phase and the particle phase is treated as a series of discrete elements; the simulation results give particle-scale resolution as the trajectory of each particle is traced. CFD-DEM is usually divided into two categories, namely resolved and unresolved, according to the resolution of the CFD solver. Resolved CFD-DEM treats the particle surfaces as no-slip boundary conditions and the immersed boundary method (IBM)[7,8] or fictitious domain method[9,10] can be used to simulate the fluid flow field, and thus a very fine CFD mesh should be used. In contrast, unresolved CFD-DEM uses the homogenized Navier–Stokes equations, the presence of the particles is represented by the porosity* or solids fraction, so that the particle-fluid interface is not resolved, and a minimum cell size of 1.6–3.0 times the particle diameter is required in the simulations.[11,12]

In the case of bidisperse, bimodal, or gap-graded particle systems with a relatively large size ratio, there are technical challenges

*In some publications it is also called "void fraction" or "voidage."

associated with use of both unresolved and resolved methods. If the unresolved method is applied, the first challenge is to select a suitable drag force expression to determine the fluid-particle interaction force. While empirical models for mono-disperse particles[13,14] and poly-disperse systems[15] have been used in many studies of the segregation of poly-disperse particle systems in fluidised beds, their reliability is questionable for large size ratios. The second issue in applying the method is determining the porosity (or solids fraction), which is also an important parameter required to calculate the drag force. It is difficult to calculate this accurately, or to obtain a representative value, when the CFD mesh size approaches the size of the largest particle diameter.[16] These problems become more pronounced the larger the particle size ratio of the system. While resolved CFD-DEM implementations do not require specification of a drag model, this approach has to use a mesh with a grid size that is less than $1/10$ of the diameter of the smallest particle in the system.[16] This fine resolution requirement significantly increases the computational cost and renders resolved CFD-DEM simulations unsuitable for most industrial applications. Some measures have been applied to address this issue. For example, Tsuji et al.[17] proposed a fictitious particles method in which large particles are made up of smaller fictitious particles; a numerical calibration procedure is required to determine the fictitious particle size and the fictitious volume fraction.

A recently proposed compromise solution is semi-resolved CFD-DEM,[18,19] in which the coarse particle and fine particle fractions are simulated using resolved and unresolved schemes, respectively. Note that the term "semi-resolved" CFD-DEM may also be used to refer to a method to smooth out the porosity field as in the works of Wang et al.[20,21] and Xie et al.[22] Here, when the term "semi-resolved CFD-DEM" is used we refer to a formulation in which the empirical drag model is applied to determine the fluid-particle interaction force for the fine particles only, while the fluid-particle interaction forces for the coarse particles are calculated analytically based on the fluid flow field. In this way the predictive capacity is improved compared to the unresolved CFD-DEM and the restriction on particle size ratio is removed. However, determining the porosity field for the calculations associated with the finer particles is not straightforward due to the discrepancy between the required CFD mesh sizes for the unresolved and resolved methods. In other words, the refined mesh applied to resolve the flow around the coarse particles may yield nonphysical porosity values for the fine particle domain. Currently, a solution for this issue reported in the literature is applying the Gaussian-kernel weighting function to distribute the volume of a single particle to the adjacent CFD cells.[19,23] This approach was originally proposed for unresolved CFD-DEM[24] and recently has been optimized for the poly-disperse systems.[25] However, the width of the kernel is arbitrarily determined, and is normally far greater than the particle size, to ensure the kernel magnitude does not vary significantly over the particle volume.[26,27] Moreover, there are difficulties in dealing with porosity calculations near walls (and near coarse particle surfaces), making them inflexible. A recent study by Xie et al.[22] proposed a hybrid CFD-DEM solver that uses the fictitious domain and unresolved methods to effectively simulate fluid-particle interactions across a broad spectrum of grid-to-particle size ratios; this is an improved semi-resolved method. However, the method also includes a porosity model that employs a Gaussian kernel function. Notably, Xie et al.[22] differed from Yang et al.[19] in that they only applied the kernel-based porosity model to medium-sized particles.

This article presents a two-grid semi-resolved CFD-DEM solver, in which a static mesh and a refined mesh are overlain. The static mesh is introduced to calculate the porosity field for the fine particles, while the refined mesh (refined from the static mesh) is used to estimate the porosity field for the coarse particles. This method is inspired by the two-grid approaches that have been applied in unresolved CFD-DEM simulations,[11,28,29] which have demonstrated the flexibility of a two-grid formulation. The proposed method is verified using existing simulation results obtained using a resolved CFD-DEM method.[16] The effects of mesh refinement level and the empirical drag force model adopted on the simulation accuracy are explored.

The paper is organized as follows: in Section 2, the formulation of the semi-resolved CFD-DEM is presented; in Section 3, the porosity calculation method using two mesh grids is shown; the approach to calculate and postprocess the fluid-particle interaction forces is given in Section 4, followed by an introduction to the simulation setup in Section 5. The performance of the proposed solver is evaluated in terms of the solid volume conservation, accuracy of the fluid-particle interaction force prediction, *etc*. in Section 6; Finally, the conclusions and the aspects for future improvement are laid out in Section 7.

## 2 | GOVERNING EQUATIONS FOR THE SEMI-RESOLVED CFD-DEM

The governing equations of the semi-resolved solver can be derived by combining the governing equations of the resolved and unresolved solvers. First, we briefly introduce the schemes adopted in each of these two solvers.

### 2.1 | Resolved solver

The CFD approach used in the resolved solver is known as the fictitious domain method,[30,31] which is the general form of the IBM. The success of this approach hinges on the ability to enforce a no-slip boundary condition on the particle surface; this can be achieved through various methods such as correcting the velocity field or applying a momentum source term. Additionally, the flow field within the solid object is also solved. The equations for the resolved solver assume incompressible fluid flow. The continuity and momentum equations are

$$\nabla \cdot \mathbf{u}_f = 0, \tag{1}$$

$$\rho_f \frac{\partial \mathbf{u}_f}{\partial t} + \rho_f (\mathbf{u}_f \cdot \nabla)\mathbf{u}_f = -\nabla p + \mu \Delta \mathbf{u}_f + \rho_f \mathbf{g}, \tag{2}$$

where $\rho_f$ and $\mathbf{u}_f$ are the density and velocity of the fluid, respectively, and $\mathbf{g}$ is acceleration due to gravity. The most important condition is

that the following no-slip conditions should be fulfilled at the fluid-particle interfaces:

$$\mathbf{u}_f = \mathbf{u}_l, \quad \text{in } \Omega_p, \tag{3}$$

where $\Omega_p$ is the region occupied by the particle or the so-called fictitious domain, and $\mathbf{u}_l$ is the local particle velocity in a CFD cell, given by:

$$\mathbf{u}_l = \mathbf{u}_p + \boldsymbol{\omega}_p \times \mathbf{r} \quad \text{in } \Omega_p, \tag{4}$$

where $\mathbf{u}_p$ and $\boldsymbol{\omega}_p$ are the translational and the angular velocity of the particle.

A resolved solver has been implemented in the official release in CFDEM,[32] with details provided in Reference 10. The procedure to implement the no-slip boundary is relatively complicated: the fluid velocity in the region occupied by the coarse particles is corrected directly based on the particle velocity field ($\mathbf{u}_l$) and the gradient of a correction factor $\psi$, from which the resulting velocity field is calculated as:

$$\bar{\mathbf{u}}_f = \mathbf{u}_l - \nabla\psi. \tag{5}$$

In order to make $\bar{\mathbf{u}}_f$ divergence-free, that is, $\nabla \cdot \bar{\mathbf{u}}_f = 0$, $\psi$ fulfills the following condition:

$$\Delta\psi = \nabla \mathbf{u}_l, \tag{6}$$

In addition to correcting the velocity field, Hager[10] also suggested expanding the pressure $p$ by the term $\frac{\partial\psi}{\partial t}$ to match the momentum equation.

However, the algorithms mentioned above are not capable of achieving no-slip boundary conditions. In fact, Equation (5) shows that there is a noticeable velocity difference between the fluid and particles within the fictitious domain ($\Omega_p$). It has been found that a good solution to overcome this limitation is direct application of the body force term $\mathbf{S}_{\text{pf}}^{reso}$, estimated based on the velocity difference between the particle and fluid, to achieve a no-slip boundary condition. This approach has been successfully employed in previous studies, such as References 9 and 33 The momentum equation (Equation 2) is rewritten as

$$\rho_f \frac{\partial \mathbf{u}_f}{\partial t} + \rho_f(\mathbf{u}_f \cdot \nabla)\mathbf{u}_f = -\nabla p + \mu\Delta\mathbf{u}_f - \mathbf{S}_{\text{pf}}^{\text{reso}} + \rho_f \mathbf{g}, \tag{7}$$

In order to get the source term $\mathbf{S}_{\text{pf}}^{\text{reso}}$, $\tilde{\mathbf{u}}_f$ should be obtained firstly without considering the presence of the particles by solving

$$\rho_f \frac{\partial \tilde{\mathbf{u}}_f}{\partial t} + \rho_f(\tilde{\mathbf{u}}_f \cdot \nabla)\tilde{\mathbf{u}}_f = -\nabla p + \mu\Delta\tilde{\mathbf{u}}_f + \rho_f \mathbf{g}, \tag{8}$$

Then $\mathbf{S}_{\text{pf}}^{\text{reso}}$ is calculated by

$$\mathbf{S}_{\text{pf}}^{\text{reso}} = \frac{(1-\varepsilon_f^{\text{reso}})(\mathbf{u}_p^{\text{reso}} - \tilde{\mathbf{u}}_f)}{\Delta t_{CFD}}, \tag{9}$$

$\mathbf{S}_{\text{pf}}^{\text{reso}}$ is nonzero only in regions occupied by particles (represented by a porosity $\varepsilon_f^{\text{reso}} < 1$) and thus eliminates the need for explicit calculation of the Lagrangian multiplier. We verify this method in Section 6.1.

## 2.2 | Unresolved solver

The equations describing the behavior of the fluid phase in the unresolved solver use the volume averaged Navier–Stokes equations, which were originally derived by Anderson and Jackson.[34] The presence of the particle phase in the fluid is represented by a porosity field ($\varepsilon_f^{\text{unreso}}$), and empirical drag models are employed to calculate the fluid-particle force. The continuity and momentum equations[5,6] are written as

$$\rho_f \frac{\partial \varepsilon_f^{\text{unreso}}}{\partial t} + \rho_f \nabla \cdot (\varepsilon_f^{\text{unreso}} \mathbf{u}_f) = 0. \tag{10}$$

$$\begin{aligned} &\rho_f \frac{\partial(\varepsilon_f^{\text{unreso}} \mathbf{u}_f)}{\partial t} + \rho_f(\varepsilon_f^{\text{unreso}} \mathbf{u}_f \cdot \nabla)\mathbf{u}_f \\ &= -\varepsilon_f^{\text{unreso}} \nabla p + \varepsilon_f^{\text{unreso}} \mu \Delta \mathbf{u}_f - \mathbf{S}_{\text{pf}}^{\text{unreso}} + \varepsilon_f^{\text{unreso}} \rho_f \mathbf{g}. \end{aligned} \tag{11}$$

The momentum source term, $\mathbf{S}_{\text{pf}}^{\text{unreso}}$ is estimated as

$$\mathbf{S}_{\text{pf}}^{\text{unreso}} = G_{\text{pf}} \mathbf{u}_f - G_{\text{pf}} \mathbf{u}_s^{\text{unreso}}, \tag{12}$$

where $G_{\text{pf}}$ is the momentum source coefficient. $G_{\text{pf}}$ is calculated as the sum of the drag forces (obtained through empirical drag models) of the particles within a CFD cell, as detailed below.

The porosity field exists in both the resolved and unresolved solvers and it is defined as the volume fraction of the fluid (gas or liquid) in a CFD cell as follows:

$$\varepsilon_f = 1 - \frac{V_s}{V_{\text{cell}}}, \tag{13}$$

where $V_s$ and $V_{\text{cell}}$ are the volume of solid material and the CFD grid cell, respectively. Figure 1 is a schematic diagram of the porosity fields ($\varepsilon_f^{\text{reso}}$ and $\varepsilon_f^{\text{unreso}}$). The value of $\varepsilon_f^{\text{reso}}$ is 0 (inside the particle) or 1 (outside the particle). The porosity is calculated for each cell in the CFD mesh. As one CFD cell contains multiple particles, the value of $\varepsilon_f^{\text{unreso}}$ of the mono-disperse particles is estimated to be in the range of $[0.37, 1.0]$ (based upon the data in Reference 35).

Along with the calculation of the $\varepsilon_f^{\text{unreso}}$ in the unresolved solver, the contribution of particle $i$ to the total solid volume in a specific CFD cell $j$ is also recorded and expressed as a weight term $W_{i,j} = \frac{V_{p,i,j}}{V_{s,tot,j}}$, which will be used to interpolate the particle proprieties to the CFD cells. This is the reason that the porosity calculation is also called "averaging" or "interpolation."[18] The interpolation scheme that maps the solid particle velocities to the CFD cells is given by

$$\mathbf{u}_{s,j} = \sum_{i=1}^{n} W_{i,j} \mathbf{u}_{p,i}. \tag{14}$$

The momentum source coefficient $G_{\text{pf,j}}$ associated with the particles in Equation (12) is obtained by interpolation to give:

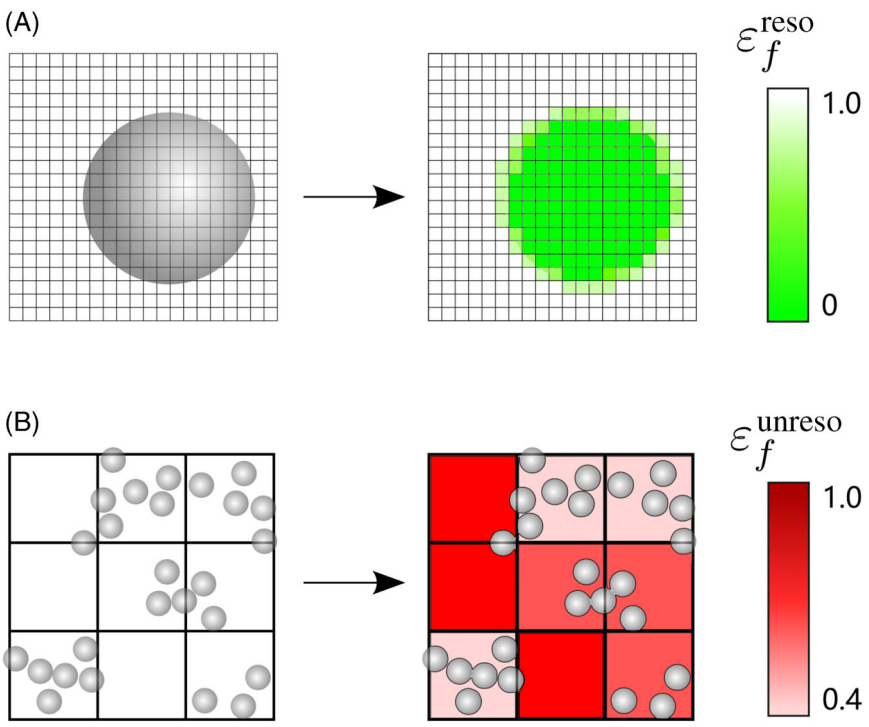


**FIGURE 1** Schematic diagram of the porosity fields in (A) resolved and (B) unresolved computational fluid dynamics coupled with the discrete element method (CFD-DEM) solvers.

$$G_{\mathrm{pf},j} = \frac{|\sum_{i=1}^{n} \mathbf{F}_{d,i} V_{p,ij}|}{V_{\mathrm{cell},j} V_{p,i} |\mathbf{u}_f - \mathbf{u}_{s,j}|}. \tag{15}$$

## 2.3 | Semi-resolved solver

The idea behind the semi-resolved solver is to extend the governing equation of the unresolved solver with a source term, $\mathbf{S}_{\mathrm{pf}}^{\mathrm{coarse}}$, as in the resolved solver, to give it the functionality of a resolved solver. The resulting equations may then be transformed into resolved or unresolved formats, depending on whether coarse or fine particles occupy the regions. This is feasible since coarse and fine particles cannot physically coexist in the same area. Referring to the above equations, the governing equations for the fluid phase in a semi-resolved solver (where flow around the coarse particles is resolved and and flow around the fine particles is not resolved) can be expressed as follows:

$$\rho_f \frac{\partial \varepsilon_f^{\mathrm{fine}}}{\partial t} + \rho_f \nabla \cdot (\varepsilon_f^{\mathrm{fine}} \mathbf{u}_f) = 0. \tag{16}$$

$$\rho_f \frac{\partial \varepsilon_f^{\mathrm{fine}} \mathbf{u}_f}{\partial t} + \rho_f (\varepsilon_f^{\mathrm{fine}} \mathbf{u}_f \cdot \nabla) \mathbf{u}_f = -\varepsilon_f^{\mathrm{fine}} \nabla p + \varepsilon_f^{\mathrm{fine}} \mu \Delta \mathbf{u}_f - \mathbf{S}_{\mathrm{pf}}^{\mathrm{fine}} + \varepsilon_f^{\mathrm{fine}} \rho_f \mathbf{g} - \mathbf{S}_{\mathrm{pf}}^{\mathrm{coarse}} \tag{17}$$

The momentum contribution from the fine particles ($\mathbf{S}_{\mathrm{pf}}^{\mathrm{fine}}$) is determined from the drag forces on the particles:

$$\mathbf{S}_{\mathrm{pf}}^{\mathrm{fine}} = G_{\mathrm{pf}} \mathbf{u}_f - G_{\mathrm{pf}} \mathbf{u}_s^{\mathrm{fine}}. \tag{18}$$

$G_{\mathrm{pf}}$ is a coefficient determined by the drag force ($\mathbf{F}_{d,i}$) on the particles, which is estimated by the empirical correlations. The contribution of the coarse particles to the momentum, $\mathbf{S}_{\mathrm{pf}}^{\mathrm{coarse}}$, is calculated according to[9,33] as

$$\mathbf{S}_{\mathrm{pf}}^{\mathrm{coarse}} = \frac{\varepsilon_f^{\mathrm{fine}} (1 - \varepsilon_f^{\mathrm{coarse}}) (\mathbf{u}_p^{\mathrm{coarse}} - \tilde{\mathbf{u}}_f)}{\Delta t_{\mathrm{CFD}}}, \tag{19}$$

where $\tilde{\mathbf{u}}_f$ is an intermediate velocity field determined without considering the immersed (coarse) particles.

The governing equations for the DEM solver are based on Newton's second law of motion and involve calculating the net force acting on each particle in the system, taking into account both contact and noncontact (fluid-particle interaction) forces. The translational and angular velocity of the particle is calculated by

$$\frac{\mathrm{d}\mathbf{u}_{p,i}}{\mathrm{d}t} = \sum_{j=1}^{N_{pp}} (\mathbf{F}_{c,ij}) + \mathbf{F}_{\nabla p,i} + \mathbf{F}_{\nabla \cdot \tau,i} + \mathbf{F}_{d,i} + m_{p,i} \mathbf{g}, \tag{20}$$

$$\mathbf{I}_i \frac{\mathrm{d}\boldsymbol{\omega}_{p,i}}{\mathrm{d}t} = \sum_{j=1}^{N_{pp}} (\mathbf{F}_{c,ij} \times (R_i \mathbf{n})) + M_{pf,i} \mathbf{t} \times \mathbf{n}, \tag{21}$$

where $\mathbf{u}_{p,i}$ is the velocity of particle $i$, $N_{pp}$ is the number of adjacent particles, $\mathbf{F}_{\nabla p,i}$, $\mathbf{F}_{\nabla \cdot \tau,i}$, and $\mathbf{F}_{d,i}$ are the pressure gradient force, viscous force and the drag force, respectively, $\mathbf{F}_{c,ij}$ is the inter-particle contact force which is calculated by the Hertz–Mindlin model.[36,37]

## 3 | TWO-GRID POROSITY METHOD

### 3.1 | Dynamic mesh refinement and porosity calculation

As mentioned earlier, difficulties still exist in calculating $\varepsilon_f^{\text{fine}}$ using semi-resolved CFD-DEM. To address this issue and improve the flexibility of the porosity calculation, a two-grid method was developed. This method utilizes two CFD grids to calculate the porosity fields; the coarse (and static) grid is used to calculate $\varepsilon_f^{\text{fine}}$. The coarse grid mesh size is 1.6 times greater than the fine particle diameter, which is in line with most methods proposed to determine the porosity such as the particle center divided method (DM).[32] The second grid, namely the dynamically refined grid used for calculating $\varepsilon_f^{\text{coarse}}$ and solving the governing equations, is generated using the *dynamicRefineFvMesh* feature in OpenFOAM. As shown in Figure 2, the strategy is to refine the mesh close to the coarse particle surface and at the same time allow as little mesh distortion as possible. It does not change the shape of the mesh cells, rather it performs topological refinements at the region where $0 < \varepsilon_f^{\text{coarse}} < 1$. The mesh refinement level (RL) is defined relative to the starting background mesh.[†] For example, if the background mesh size is 2 mm, the mesh sizes at one and two levels of refinement will be 1 and 0.5 mm, respectively. The advantage of the dynamic refinement is that it achieves a high resolution where necessary around the particles while maintaining high computational efficiency. The $\varepsilon_f^{\text{coarse}}$ field on the refined mesh grid can be estimated by a couple of methods[9,10,38] and we adopted the method proposed by Kempe et al.,[38] which is based on the signed-distance level set function of the particle surface and is easy to implement. Due to the dynamic refinement process, the size of the refined CFD grid may be smaller than the fine particles in the corresponding regions. Hence, it is not possible to estimate $\varepsilon_f^{\text{fine}}$ directly on this mesh. Therefore, a field mapping procedure is conducted to transfer the variables ($\varepsilon_f^{\text{fine}}$, $\mathbf{u}_s$, $G_{\text{pf}}^{\text{fine}}$) from the coarse grid to the fine grid, and this is introduced in the following section.

### 3.2 | Field mapping with solid volume compensation

The *mapFields* feature[‡] already available in OpenFOAM is used to perform the field mapping. Since the two grids have identical boundary conditions, and the refined mesh cells are obtained by splitting cells on the static mesh, the mapping option used is *Nearest*. This method searches for the cell in the coarse grid that is closest to the target cell in the fine grid and uses the value of the this closest cell directly in the target cell.

A difficulty in mapping the porosity field between two grids is that the volume of the particles may not be conserved, meaning that the total particle volume stored in the CFD mesh may be underestimated or overestimated. Figure 3 illustrates the field mapping procedures for $\varepsilon_f^{\text{fine}}$ from the static mesh to the refined mesh. Since $\varepsilon_f^{\text{fine}}$ was initially estimated in the static mesh (without any refinement), the values outside a coarse particle may expand into its occupied region (see Figure 3E), where the value of $\varepsilon_f^{\text{fine}}$ should be one. To avoid such errors, a solid volume compensation procedure is implemented to correct the $\varepsilon_f^{\text{fine}}$ values. The basic idea of the method is to set all the cell values in the internal area of the coarse particle to one and then compensate for the "lost" volume of fine particles by decreasing the porosity of the cells at the boundary of that coarse particle (see Figure 3F,G).

Compared to existing porosity models for semi-resolved CFD-DEM,[19] the proposed two-grid method has two key advantages. Firstly, it is highly flexible as any existing porosity calculation algorithms can be used to calculate the porosity field on the coarse grid without the need for additional treatment, and the same procedure can be applied for field mapping. Secondly, the proposed method does not require additional arbitrary input parameters such as the bandwidth in the Gaussian kernel method[19,24] or the size of the porous sphere[39] or porous cube.[40]

Along with the field mapping of $\varepsilon_f^{\text{fine}}$, the momentum source field $G_{\text{pf}}^{\text{fine}}$, and the solid velocity $\mathbf{u}_s$ are also mapped. Specifically, $G_{\text{pf}}^{\text{fine}}$ was calculated using the same weight function, based on proportion of the particle volume in each CFD cell, that was adopted to calculate $\varepsilon_f^{\text{fine}}$. As a result, a correction must be applied to $G_{\text{pf}}^{\text{fine}}$, as illustrated in Figure 3, to ensure conservation of the total momentum.

## 4 | FLUID-PARTICLE INTERACTION FORCE CALCULATION

### 4.1 | Two force calculation schemes

The fluid-particle interaction forces acting on the coarse particles can be calculated using two different methods: the direct method[9,33] and the Shirgaonkar method.[41] The direct method uses the value of the force (or momentum source term) applied in Equation (17), which is given by

$$\mathbf{F}_{pf,i}^{\text{coarse}} = \rho_f \int_{V(c)} \varepsilon_f^{\text{fine}} (1 - \varepsilon_f^{\text{coarse}}) \frac{(\mathbf{u}_{p,i} - \tilde{\mathbf{u}}_f) - (\mathbf{u}_f - \mathbf{u}_f^{prev})}{\Delta t_{\text{CFD}}} \mathrm{d}V(c). \quad (22)$$

In the Shirgaonkar method, the total fluid-particle interaction force is estimated by integrating the force over the domain occupied by the coarse particle, given by

$$\mathbf{F}_{pf,i}^{\text{coarse}} = \rho_f \int_{V(c)} \varepsilon_f^{\text{fine}} (1 - \varepsilon_f^{\text{coarse}}) (-\nabla p + \mu_f \Delta \mathbf{u}) \, \mathrm{d}V(c), \quad (23)$$

As the fluid field around the boundary of a coarse particle is resolved in the solver, according to the fluid field with a high resolution, the resulting torque due to the fluid-particle interaction can be calculated by

[†] https://www.openfoam.com/documentation/guides/latest/doc/guide-meshing-snappyhexmesh-castellation.html

[‡] https://openfoamwiki.net/index.php/MapFields

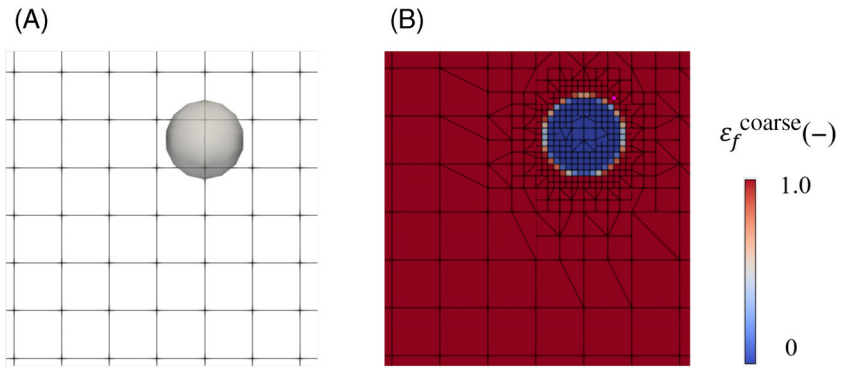


**FIGURE 2** Schematic diagram of the mesh refinement (A) static mesh (B) refined system with a mesh refinement level of 3.

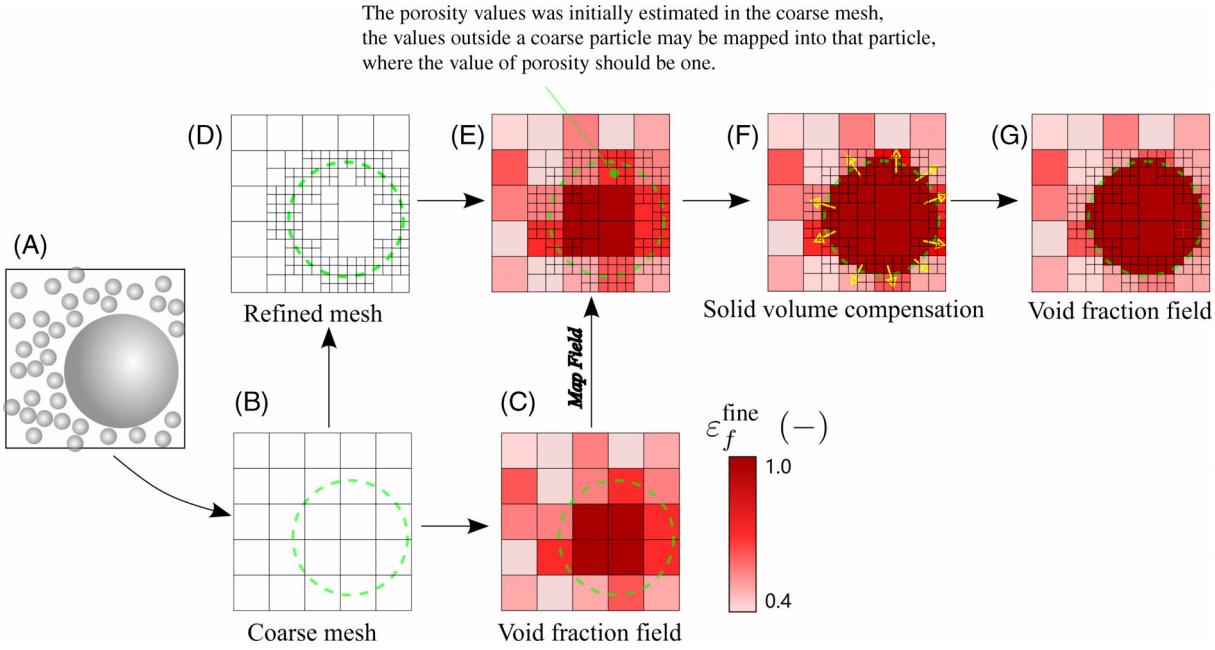


**FIGURE 3** Diagram of the field mapping with solid volume compensation approach.

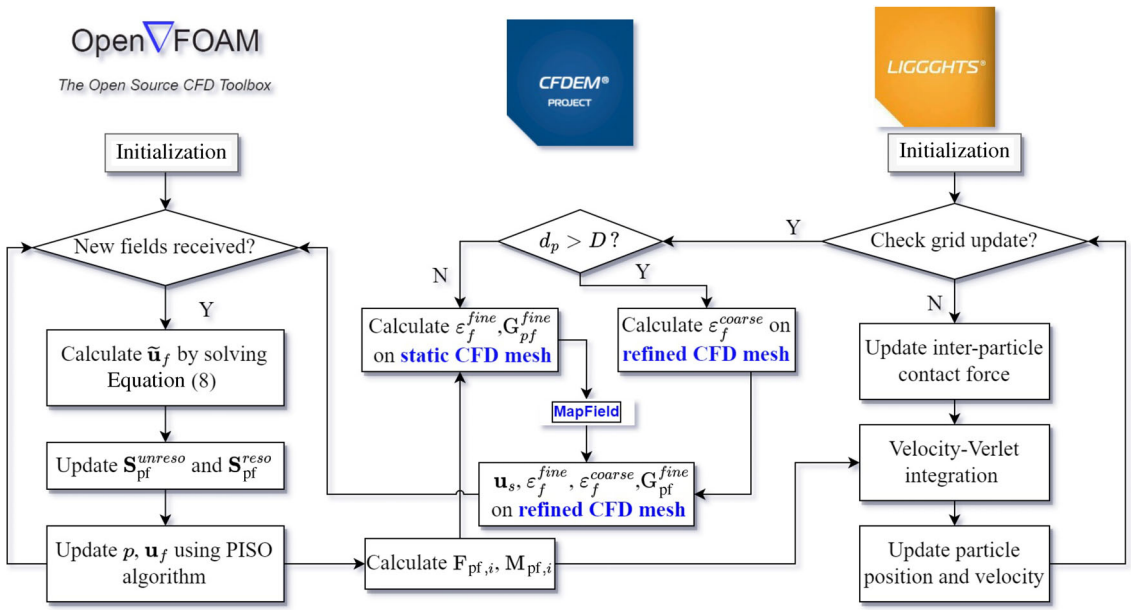


**FIGURE 4** Flowchart of the two-grid semi-resolved computational fluid dynamics coupled with the discrete element method (CFD-DEM).

$$\mathbf{M}_{pf,i}^{\text{coarse}} = \int_{V(c)} \mathbf{r} \times \mathbf{F}_{pf,i}^{\text{coarse}} \, dV(c). \quad (24)$$

## 4.2 | Fluid-particle interaction force normalization

In the following text, $\mathbf{F}_{pf,i}$ is chosen for comparison with the resolved simulation because it is easily obtained from both solvers and is directly related to particle motion. To facilitate better visualization of the fluid-particle interaction force, all the particle-fluid interaction forces discussed in the following are normalized by the Stokes force as

$$\bar{\mathbf{F}}_{pf,i} = \mathbf{F}_{pf,i} / \mathbf{F}_{pf,i}^{Stokes} = \mathbf{F}_{pf,i} / (3\pi\mu d_p |\mathbf{u}_f - \mathbf{u}_{p,i}|). \quad (25)$$

# 5 | SIMULATION SETUP

The semi-resolved solver was implemented in the CFD-DEM open-source code CFDEM,[32] which couples the CFD solver OpenFOAM[42] and the DEM solver LIGGGHTS.[32] Figure 4 shows the flow chart of the implemented algorithm.

The semi-resolved solver outlined here is suitable for bi-modal or gap-graded particle systems with a large size ratio. In order to rigorously evaluate the accuracy and efficiency of the solver, previously obtained resolved simulation results from Knight[16] were used for a bi-modal particle assembly with a particle size ratio of 4.0. Table 1 displays the overall configuration of Knight's simulation cases, where particle assemblies with a fine particle volume fraction ($f_{\text{fine}}$) ranging from 0.11–0.51 were selected. The coupling interval, that is, the period in which the two solvers exchange information, was set to $100\Delta t_{\text{DEM}}$.

The procedures for performing the immersed boundary simulations have been outlined in previous contributions.[16,43] Here, we provide only a high-level description. Initially, particles were randomly placed within cubic periodic boundaries to create the samples. Then, the sample was subjected to increasing isotropic compression up to an effective stress of 100 kPa in the DEM solver using servo-controlled periodic boundaries.[44] During laminar flow, the fluid-particle interactions were determined by IBM simulations using the Multiflow code.[8,45]

Figure 5 shows the particle assembly considered, with a particle size ratio of 4. In the CFD solver, the boundaries in the $y$ and $z$ direction are periodic. In the $x$-direction, the inlet boundary has a fixed fluid velocity and zero pressure gradient, and the outlet has a fixed pressure of zero. Periodic boundaries are also applied in the DEM solver. The sample is fixed in space and the particles do not move during the simulation. Table 2 lists the particle properties and numerical settings in the semi-resolved CFD-DEM simulations. As the "divided" porosity model is used to estimate $\varepsilon_f^{\text{fine}}$, the static mesh size should be greater than the fine

**TABLE 1** Overall configuration of the particle assemblies for the semi-resolved CFD-DEM verification.

| Case | $f_{\text{fine}}(-)$ | $\phi(-)$ | $N_{\text{total}}(-)$ | $N_{\text{coarse}}(-)$ |
|---|---|---|---|---|
| 1 | 0.11 | 0.645 | 317 | 38 |
| 2 | 0.25 | 0.648 | 696 | 32 |
| 3 | 0.51 | 0.621 | 1363 | 21 |

*Note*: Coarse-fine particle size ratio was four in all cases.

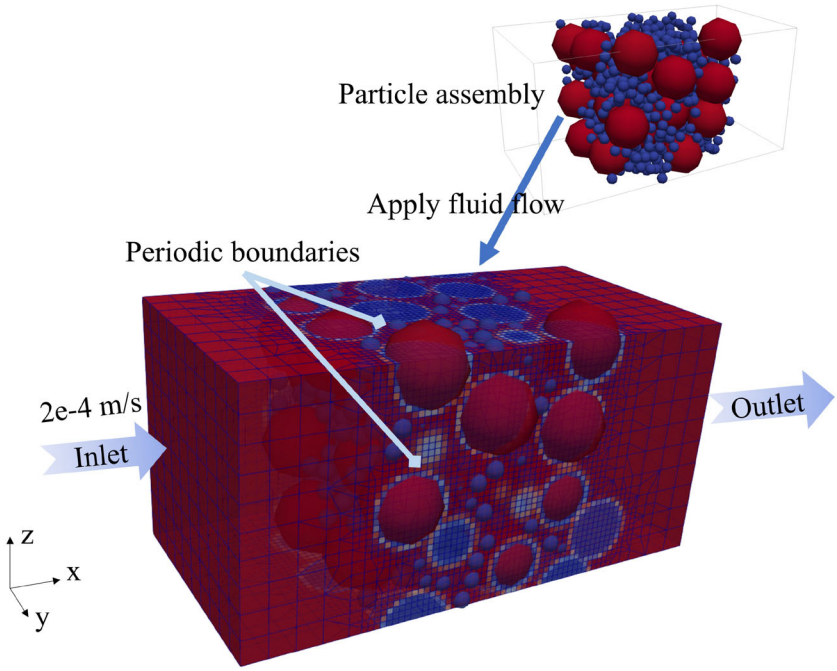


**FIGURE 5** Illustration of particle assembly considered (with a coarse-fine particle size ratio of 4) including annotation of boundary conditions.

particle diameter.[32] Thus mesh-particle size ratio (SR) of 1.6 was chosen to generate the background static mesh. In order to capture the pore fluid flow around the coarse particle, the mesh near the boundary of the coarse particles is dynamically refined with a refinement level of 2 to 4. The simulations were terminated when the pressure drop across the particle assembly reached a stable level; then the total fluid-particle interaction force ($\mathbf{F}_{pf,i}$) was extracted from the particle data directly.

While the primary focus of this paper is to assess the computational cost of the semi-resolved method using existing high-accuracy resolved CFD-DEM simulations, an additional spouted bed simulation was conducted to evaluate the model's feasibility with moving particles. Figure 6 illustrates the spouted bed cases. A spouted bed is a gas-solid reactor widely used in chemical and food engineering, characterized by the presence of an internal particle circulation driven by the spouted region at the center of the bed. The geometry and input parameters for the spouted bed were based on Link's work,[40] which has served as a benchmark case for numerous numerical studies.

As depicted in Figure 6, the air velocity within the spouted region was 30 m/s, with a total of 24,500 particles having a density of 2505 kg/m$^3$ present in the bed. Additionally, a coarse particle, five times larger in diameter than the fine fraction, was introduced into the simulation. Further details on the input parameters can be found in References 40 and 46.

**TABLE 2** Parameters of the particles in the semi-resolved CFD-DEM verification cases.

| Property | Value | Unit |
|---|---|---|
| Density ($\rho_p$) | 2470 | kg/$m^3$ |
| Coefficient of restitution ($e$) | 0.5 | - |
| Coulomb friction coefficient ($\mu$) | 0.3 | - |
| Inlet velocity ($U$) | $2\times10^{-4}$ | m/s |
| Time step of CFD ($\Delta t_{CFD}$) | $5\times10^{-6}$ | s |
| Time step of DEM ($\Delta t_{DEM}$) | $5\times10^{-8}$ | s |
| Coupling interval | 100 | - |

## 6 | RESULTS AND DISCUSSION

### 6.1 | Verification of the resolved solver: laminar flow through ordered packings

As mentioned in Section 2.1, the resolved solver now includes a new FD (or IBM) method to improve accuracy. To ensure the accuracy of the semi-resolved method based on IBM, this new method must be fully verified. verification cases involve ordered packings of mono-disperse spheres at low Reynolds numbers. Analytical solutions for these packings, including periodic simple cubic (SC), body-centered cubic (BCC), and face-centered cubic (FCC) arrays, have been provided by Zick and Homsy,[47] and

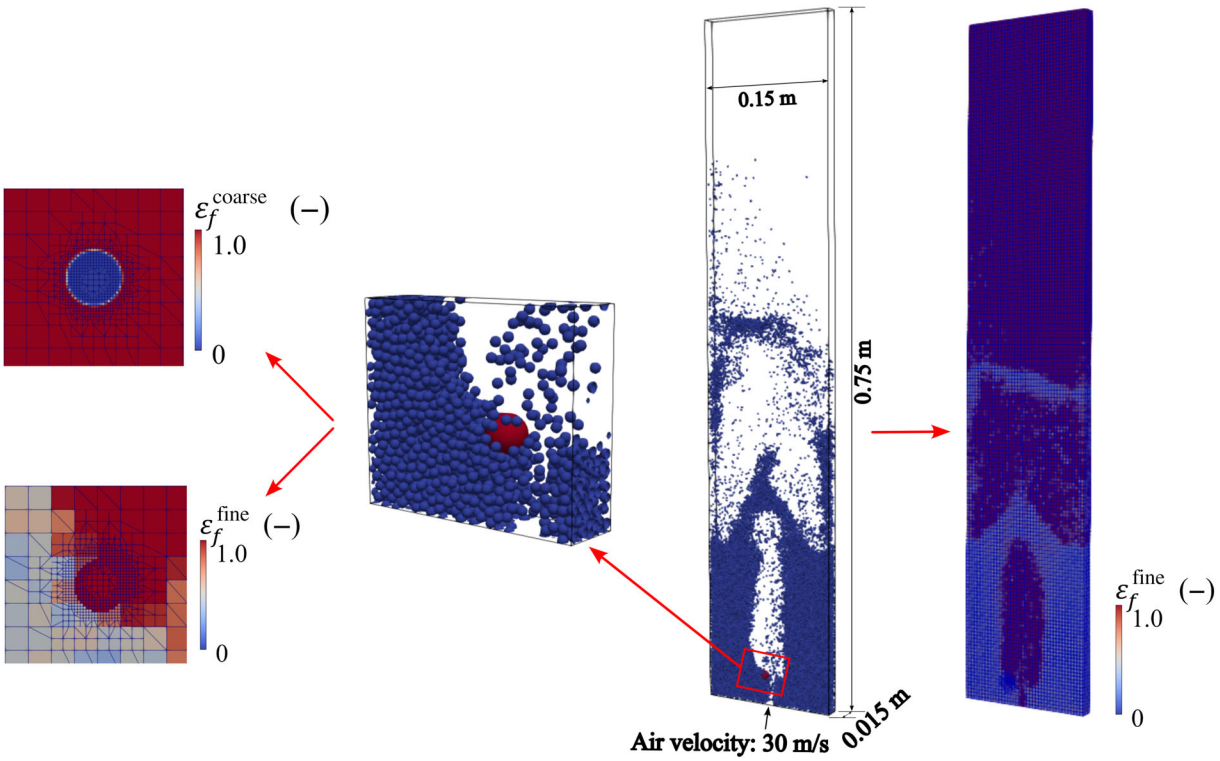


**FIGURE 6** Schematic of the spouted bed.

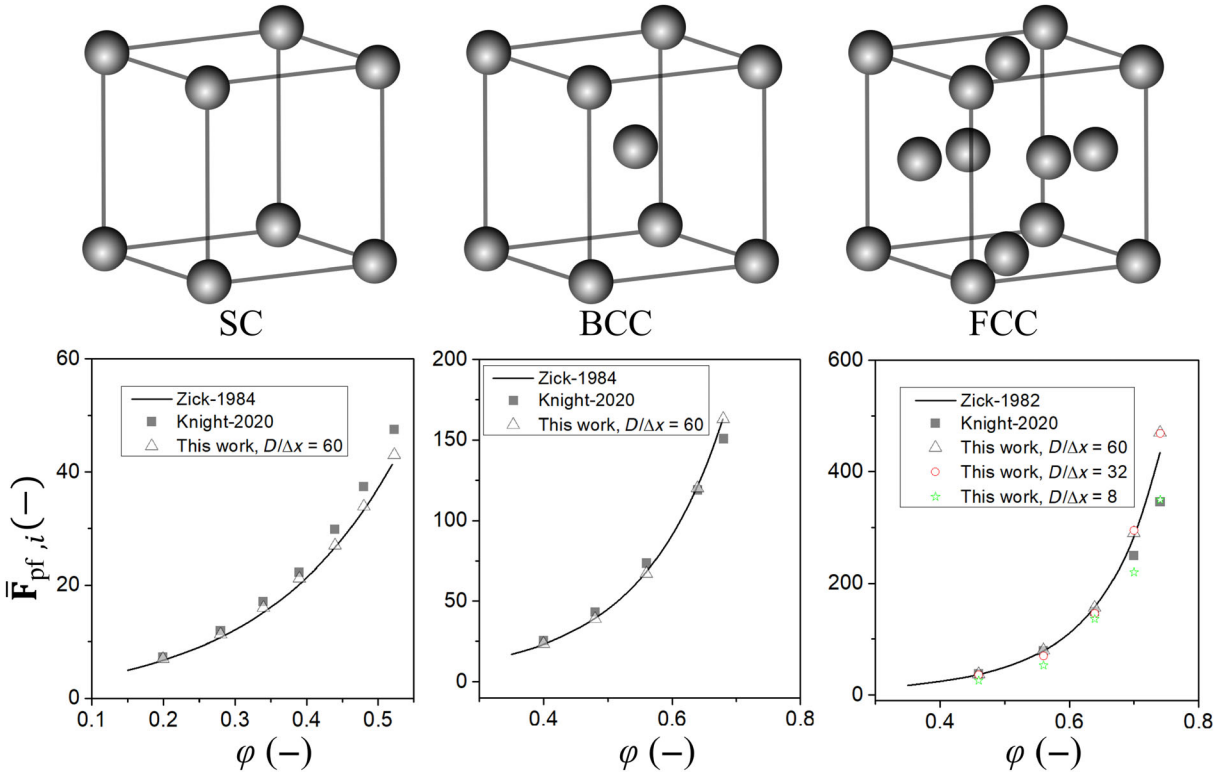


**FIGURE 7** Comparison of the normalized fluid-particle force for lattice packings of uniform spheres: left to right considers simple cubic (SC), body centered cubic (BCC) and face centered cubic (FCC) packing configurations.

these data have been used by several researchers for benchmark verification purposes.[48–50] Figure 7 shows the variation of $\mathbf{F}_{pf,i}$ with $\phi$ for SC, BCC, and FCC arrays predicted by analytical results,[47] IBM simulations (taken from Reference 43 with the radius retraction parameter of 0.2 and $D/\Delta x = 64$) and the current work ($D/\Delta x = 8, 32, 60$), where $D$ is the particle diameter and $\Delta x$ is the grid size. Both sets of simulation data almost coincide with the analytical results, with a slight discrepancy in cases with high solid fraction. Moreover, from the FCC data, it is obvious that when $D/\Delta x = 32$, a high simulation accuracy can still be achieved, but the values of $\mathbf{F}_{pf,i}$ are all slightly underestimated when $D/\Delta x$ is reduced to 8. Knight et al.[43] discussed the suitability of the IBM for predicting particle-fluid interaction of ordered packings. Although the accuracy of the IBM method is somewhat lower than some of the more refined calculation methods such as unstructured mesh methods, it strikes a good balance between computational cost and accuracy.

## 6.2 | Effect of mesh refinement levels

### 6.2.1 | Solid volume conservation

The field mapping approach with particle volume compensation was evaluated by comparing the total solid volume of the fine fraction in the CFD mesh before and after applying the compensation. For the Case 1 particle assembly of Case 1 shown in Figure 5, the results are shown in Figure 8, where the y-axis represents the ratio between the total solid volume in the CFD mesh and the real solid volume of the particle assembly. There is a relatively high error (>13%) in the solid volume for the cases that do not use the solid volume compensation algorithm. However, after applying the modification, these errors are reduced to be lower than 0.1%. This indicates that the solid volume compensation algorithm is necessary and accurate for ensuring the accuracy of the field mapping approach.

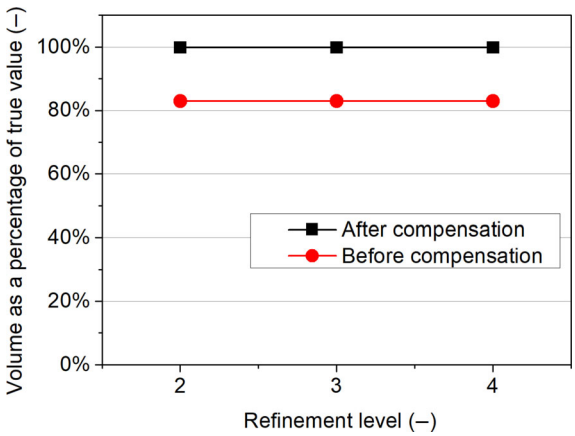


**FIGURE 8** Comparison of the total fine particle volume obtained from the porosity model with and without applying the solid volume compensation.

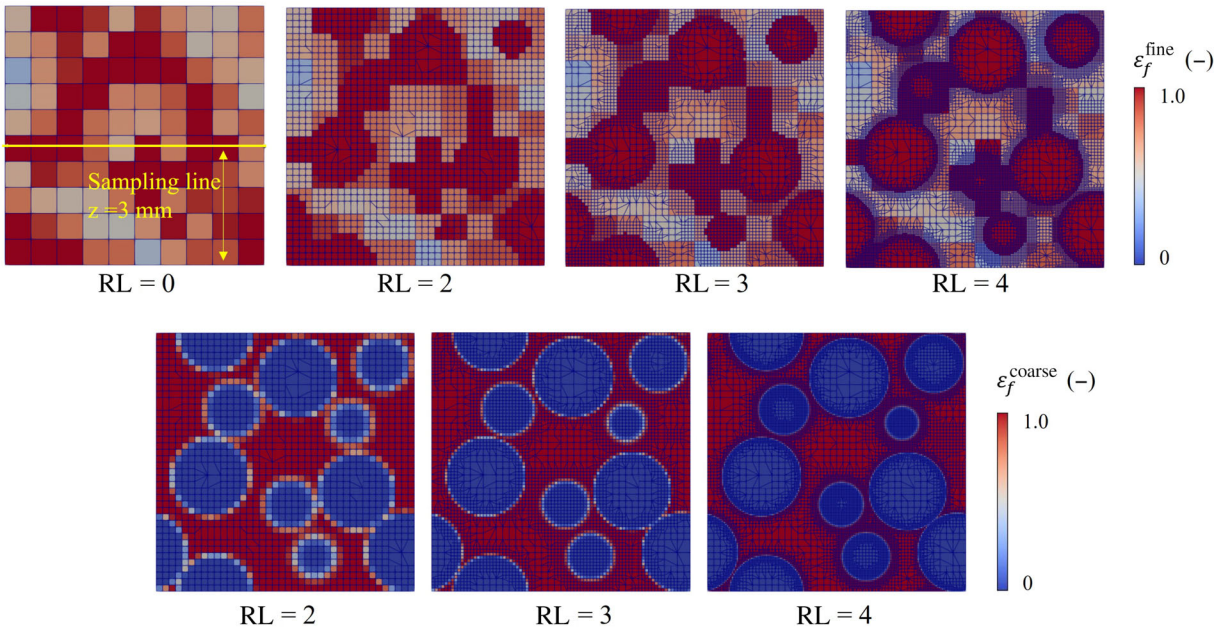


**FIGURE 9** $\varepsilon_f^{coarse}$ and $\varepsilon_f^{fine}$ fields under different mesh refinement levels (the slice was taken in the y-z plane at a distance of 0.33 cm from the inlet, the size ratio of particles in the sample is 4).

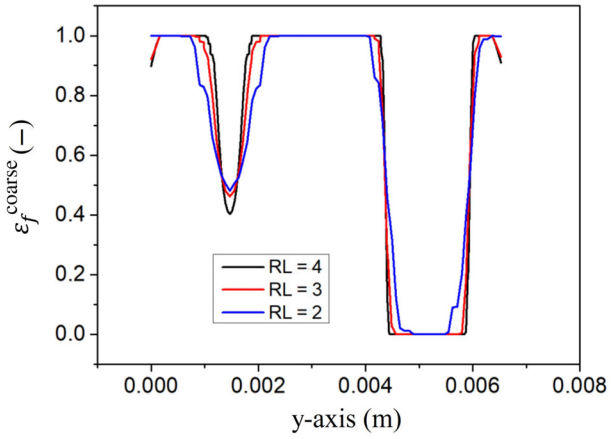


**FIGURE 10** Variation in $\varepsilon_f^{coarse}$ for successive slices in the x-z plane along a straight line parallel to the y-axis (as indicated in 9) for three different mesh refinement levels (RLs).

Figure 9 shows the distributions of $\varepsilon_f^{fine}$ and $\varepsilon_f^{coarse}$ with different refinement levels on a slice through the domain in the y-z plane at a distance of 0.33 cm from the inlet. Figures 10 and 11 show the variation in $\varepsilon_f^{coarse}$ and $\varepsilon_f^{fine}$ along a straight line (as indicated in Figure 9). As Figure 11 indicates, due to the low resolution in the coarse CFD grids, the $\varepsilon_f^{fine}$ field cannot represent the fine particle distribution correctly without the dynamic mesh refinement. As the dynamic cell refinement level increases, the porosity fields at the boundary region of the coarse particle sharpen and the curves become closer, in other words the local porosity at the edge of the coarse particles is captured more accurately as RF increases. The difference between them becomes less pronounced when RL ≥ 3.

### 6.2.2 | Particle-fluid interaction force

Figure 12 compares the total fluid-particle interaction forces calculated from the resolved and the semi-resolved methods for refinement levels (RL) of 2, 3, and 4 considering both the fine and coarse particles. Given the proximity of the results across different RL values, the data is presented in a log-log plot to more distinctly highlight the variations between these cases. Table 3 shows the corresponding Pearson correlation (PC)[§] between the fluid-particle interaction forces calculated from these two methods. The *PC* is a variable that measures linear correlation between two sets of data, and it has been used to assess the accuracy of simulating fluid-particle interaction forces in a previous study.[46] A *PC* value of 1 indicates that the two sets of data are identical. As the *RL* increases from 2 to 3, the $PC_{coarse}$ increases by 0.144 to 0.746; as the *RL* further increases to 4, the $PC_{coarse}$ increases by approximately 0.04 to 0.781, which is a minor change compared with the former case. This suggests that the mesh has been refined adequately to capture the details, and further mesh refinement is unlikely to impact simulation accuracy. In contrast, the change in the $PC_{fine}$ is not pronounced under different *RL* values. Therefore, mesh refinement can improve the accuracy of $\mathbf{F}_{pf,i}^{coarse}$ until a specific *RL* has been reached, but the accuracy of the $\mathbf{F}_{pf,i}^{fine}$ is not affected in this process. This result is not surprising for two reasons. Firstly, the refinement of the CFD meshes helps to improve the accuracy of the fictitious domain method, as it is recommended that the mesh size should be smaller than 1/10 of the particle diameter for the resolved solver; secondly, the $\mathbf{F}_{pf,i}^{fine}$ is computed using empirical drag force correlations (such as Ergun, Tang, etc.) and are based on

[§]https://real-statistics.com/correlation/basic-concepts-correlation/

the fluid velocity on the static mesh, which is obtained by spatially averaging the velocity field on the refined mesh with higher resolution.Therefore, while the resolution of flow field calculation can be improved by refining the CFD meshes, its impact on the final prediction of forces acting on fine particles is expected to remain limited.

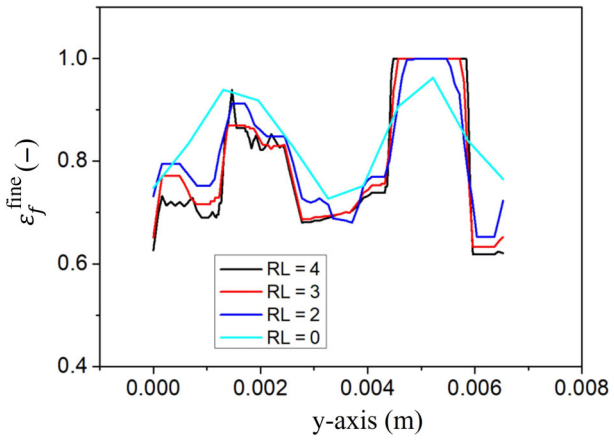


**FIGURE 11** Variation in $\varepsilon_f^{fine}$ for successive slices in the x-z plane along a straight line parallel to the y-axis (as indicated in 9) for three different mesh refinement levels (RLs).

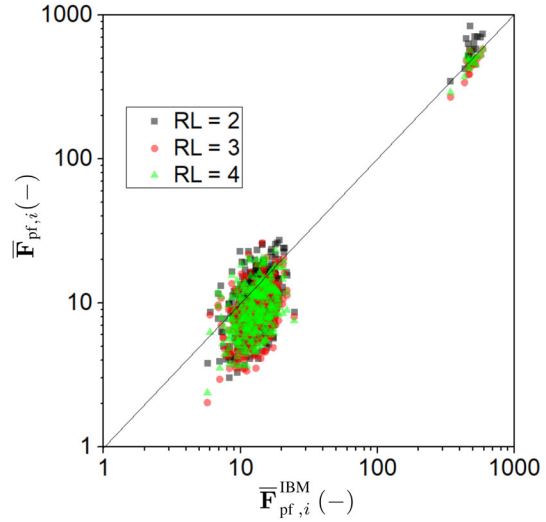


**FIGURE 12** Comparison of the total particle-fluid interaction force estimated using computational fluid dynamics (CFD) meshes with refinement levels of 2, 3, and 4. (Inset illustrates the force data for the fine particles).

## 6.3 | Effect of coarse particle force model

The $\mathbf{F}_{pf,i}^{coarse}$ calculated using the above mentioned two force calculation methods (see Equations 22 and 23) is compared in Figure 13. Though Shirgaonkar's method results in slightly lower force values, the differences are minor. This characteristic is evident in Table 3, where the values of $PC_{coarse}$ obtained through these two methods exhibit very little variation. Furthermore, it was observed that the computational costs of these two methods are remarkably similar, with simulation times of 40,075 s for Shirgaonkar's method and 40,379 s for the Direct method, both corresponding to a physical time of 0.1 s (RL = 3). The two force models are derived using different ideas and show close results, which again reflects the reliability of the present solver.

## 6.4 | Effect of the empirical drag model

The proposed semi-resolved solver calculates the drag force on the fine particles using an empirical model. However, the calculated drag forces impact the flow field and so the sensitivity of both $\mathbf{F}_{pf,i}^{coarse}$ and $\mathbf{F}_{pf,i}^{fine}$ to the drag model must be considered. In order to evaluate the effect of the drag expression adopted on the simulation accuracy, the empirical models of Ergun,[51] Di

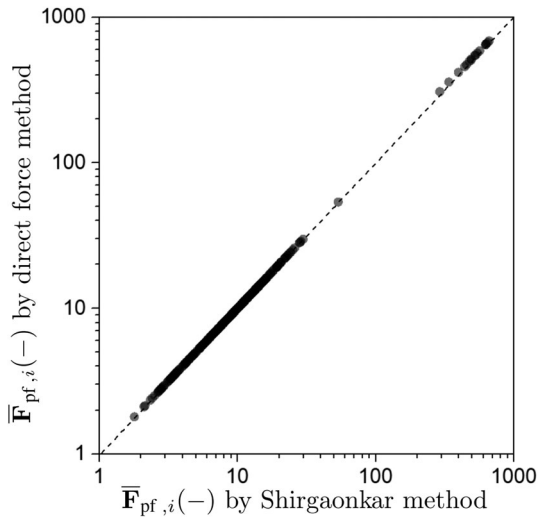


**FIGURE 13** Comparison of the fluid-particle force acting on the coarse particles predicted by the direct method and the Shirgaonkar method.

**TABLE 3** Pearson correlation of $\mathbf{F}_{pf,i}$ comparing data from the resolved (IBM) and semi-resolved solvers for different *RL* values.

| *RL*(−) | $N_{cell}(-)$ | Ratio (-) | $\mathbf{F}_{pf,i}$ models: Fine/Coarse | $PC_{fine}(-)$ | $PC_{coarse}(-)$ |
|---|---|---|---|---|---|
| 2 | 100,596 | 6.15 | Ergun/Shirgaonkar | 0.605 | 0.602 |
| 3 | 655,453 | 12.30 | Ergun/Shirgaonkar | 0.618 | 0.746 |
| 4 | 3,369,032 | 24.60 | Ergun/Shirgaonkar | 0.606 | 0.781 |
| 3 | 655,453 | 12.30 | Ergun/Direct | 0.618 | 0.746 |

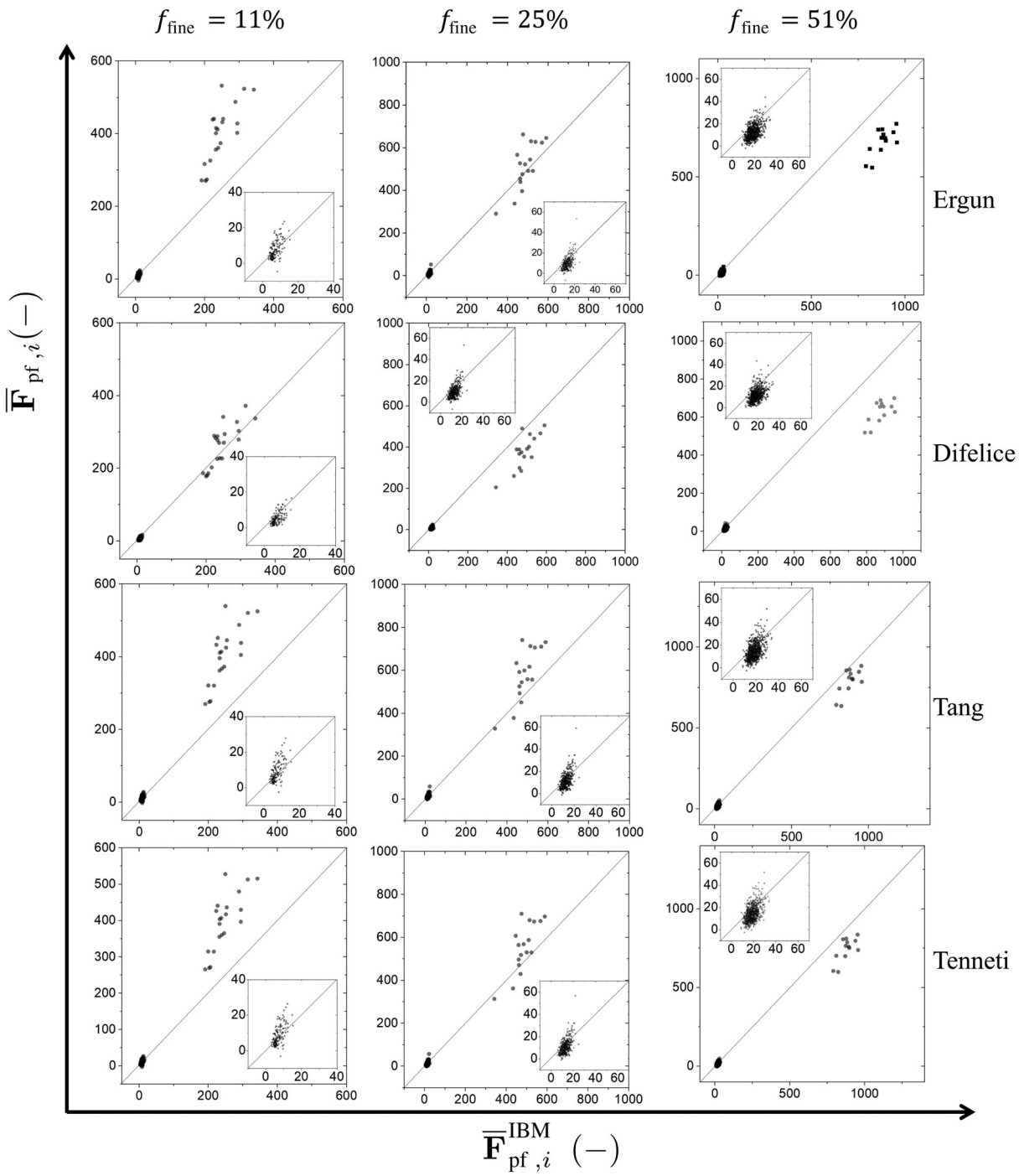


**FIGURE 14** Comparison of the $\mathbf{F}_{\text{pf},i}$ from resolved and semi-resolved solvers illustrating sensitivity to the drag model adopted for the finer particles (inset gives magnified image of data for the finer particles).

Felice,[52] Tang[53] and Tenneti[50] were applied in the simulation cases with bi-modal samples. These drag expressions were chosen as they have previously been applied to similar systems.[16,46] Figure 14 compares the calculated fluid particle interaction force with values from the resolved solvers; Figure 15 shows the mean and the standard deviation (SD) values of $\mathbf{F}_{pf,i}$, and the Pearson correlation coefficient (PC) of the corresponding case is also listed in Table 4. For each case, the data for the fine and coarse particles are shown separately. After a careful analysis of those data, the following conclusions emerged. (i) For cases with $f_{\text{fine}} = 11\%, 25\%$ and $50\%$, adopting the Di Felice, Ergun and Tang models led to the best match for $\mathbf{F}^{\text{coarse}}_{\text{pf},i}$ data, and Ergun, Tang and Tenneti models provided the best match for the $\mathbf{F}^{\text{fine}}_{\text{pf},i}$ data, respectively. (ii) In all cases, the values of $\text{PC}_{\text{fine}}$ are relatively low (<0.62) and show more scatter compared to the IBM data (with lower SD), which indicates that the stability of this approach to accurately predict $\mathbf{F}^{\text{fine}}_{\text{pf},i}$ is low. This result

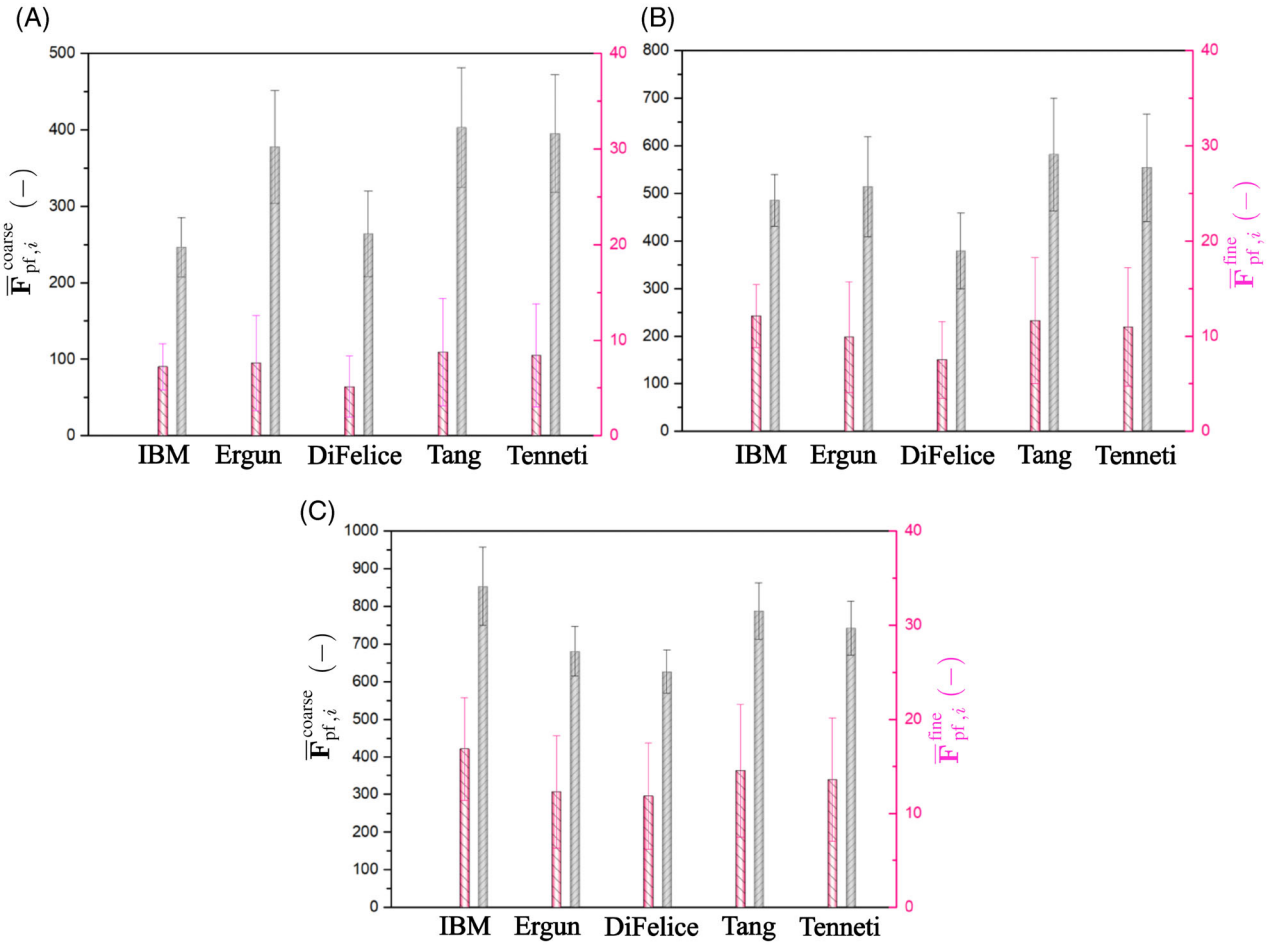


**FIGURE 15** Comparison of the $\mathbf{F}_{pf,i}$ from the existing resolved and semi-resolved solvers for Cases 1–3 ($f_{fine} = 0.11, f_{fine} = 0.25, f_{fine} = 0.51$), data for immersed boundary method (IBM) simulations presented alongside semi-resolved data obtained using different empirical drag coefficients to calculate $\mathbf{F}^{fine}_{pf,i}$.

**TABLE 4** Pearson correlation of $\mathbf{F}_{pf,i}$ comparing the resolved (IBM) and semi-resolved solvers for the different emprical drag models that were applied to calculate $\mathbf{F}^{fine}_{pf,i}$.

| | $f_{fine} = 0.11$ | | $f_{fine} = 0.25$ | | $f_{fine} = 0.51$ | |
|---|---|---|---|---|---|---|
| **Empirical models** | **Coarse** | **Fine** | **Coarse** | **Fine** | **Coarse** | **Fine** |
| Ergun | 0.78 | 0.60 | 0.76 | 0.54 | 0.70 | 0.49 |
| Difelice | 0.80 | 0.62 | 0.79 | 0.45 | 0.67 | 0.44 |
| Tang | 0.77 | 0.62 | 0.77 | 0.55 | 0.71 | 0.48 |
| Tenneti | 0.77 | 0.62 | 0.77 | 0.55 | 0.70 | 0.49 |

is not surprising as the empirical correlations were used to calculated the drag force (and thus the $\mathbf{F}_{pf,i}$) for the fine particles in each case. Previous studies[43,46] have indicated that though the empirical drag correlations (for a mono-disperse particle system) can provide a good approximation to the overall drag force, they deliver a poor performance in the fluid-particle interaction force prediction for individual particles compared to the IBM simulations. In contrast, the fluid flow is resolved around the surface of the coarse particles, the $\mathbf{F}^{coarse}_{pf,i}$ was calculated directly and thus $PC_{coarse}$ are higher than $PC_{fine}$. We emphasize that the semi-resolved solver is mainly proposed to improve the feasibility and accuracy of the interaction between the coarse particle and the fluid flow.

## 6.5 | Effect of the particle motion

In order to explore the effect of the particle motion on the proposed porosity model with the dynamic mesh refinement, the transient

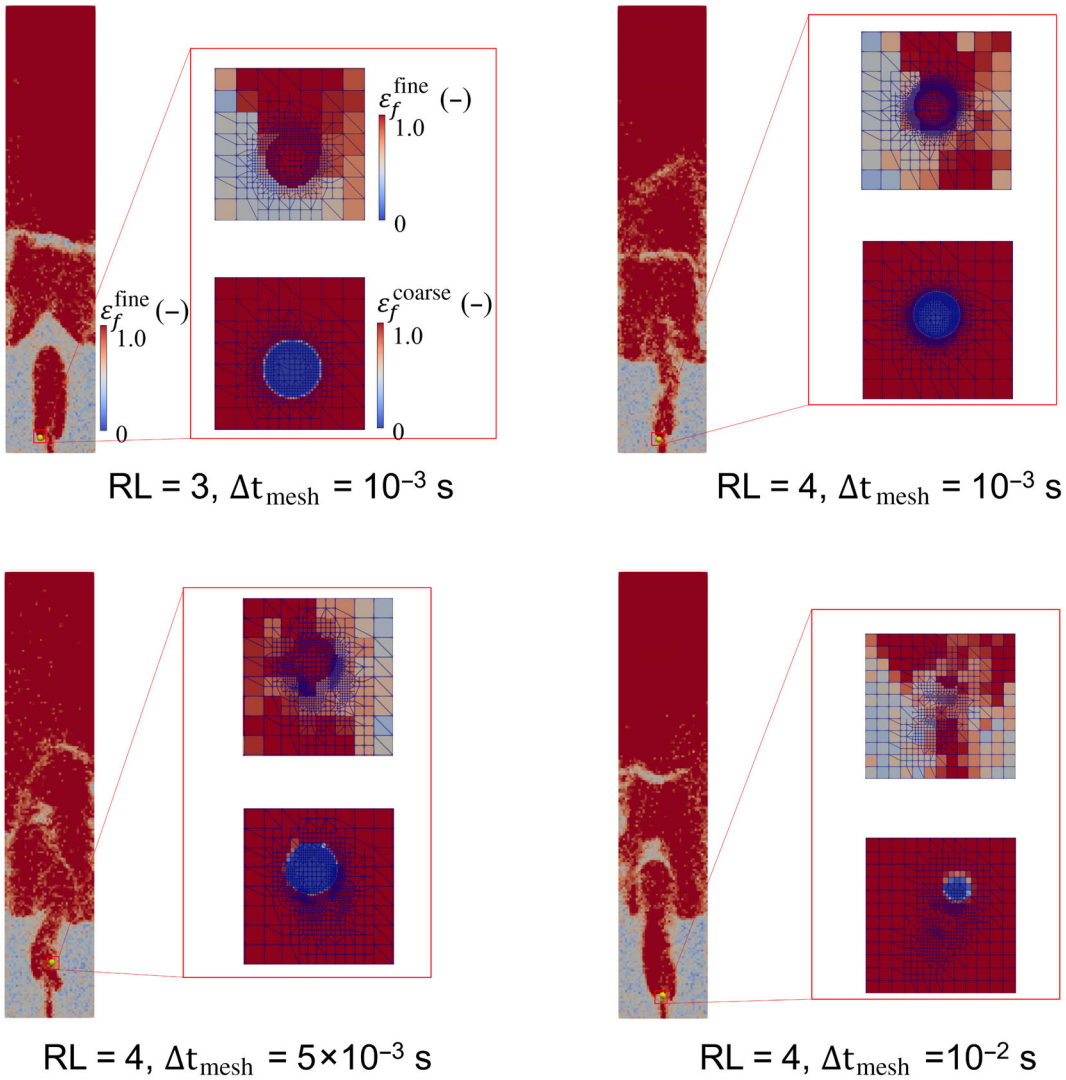


**FIGURE 16** Transient mesh refinement around the coarse particle.

refined meshes around the coarse particle in the spouted bed are depicted in Figure 16. The transient x-y slices of the porosity fields when the coarse particle situated at the center of the spouted region was chosen for each scenario, showcasing the mesh refinement interval's capability to accurately capture high-speed particle motion. In the cases where the mesh updating interval ($\Delta t_{mesh}$) was set to 0.001 s (RL = 3, 4), the mesh refinement effectively tracked the particle motion. However, as the mesh updating interval increased, the mesh refinement fell behind the particle's motion (Figure 16C,D), leaving parts of the region covered by the coarse particle insufficiently refined.

A straightforward yet efficient method for estimating the maximum mesh refinement interval relies on the maximum particle velocity ($u_p^{max}$) and the distance of the buffer layers ($L_{buffer}$) in the refined mesh. For instance, in this particular case, the updating rate can be calculated as $L_{buffer}/u_p^{max} \approx 0.002$ s. Therefore, the updating rates of 0.01 and 0.005 s are deemed too lengthy.

## 6.6 | Computational efficiency and accuracy

From a computational standpoint, an essential criterion for any semi-resolved CFD-DEM implementation is its ability to reduce the computational cost compared to resolved cases. Resolved simulations for bi-modal particle assemblies, for example, typically require $10^6$ to $10^7$ fluid cells and 12 to 48 h to reach steady-state flow conditions on 100 to 1000 processing units, as the mesh cell size should be smaller than one-tenth of the smallest particle diameter in the flow system. Such a high computational cost confirms that resolved solvers are not suitable for real industrial simulations. In contrast, all the semi-resolved simulations presented in this paper were run using $10^5$ to $10^6$ fluid cells (under mesh refinement levels of 3 to 4, see Table 3), requiring 2 to 10 h to reach steady-state flow conditions on 4 to 12 processing units. The computational cost can be roughly estimated based on the number of CFD cells, as the calculation loads are mainly spent on the CFD solver side. The mesh cell number is only 1% to

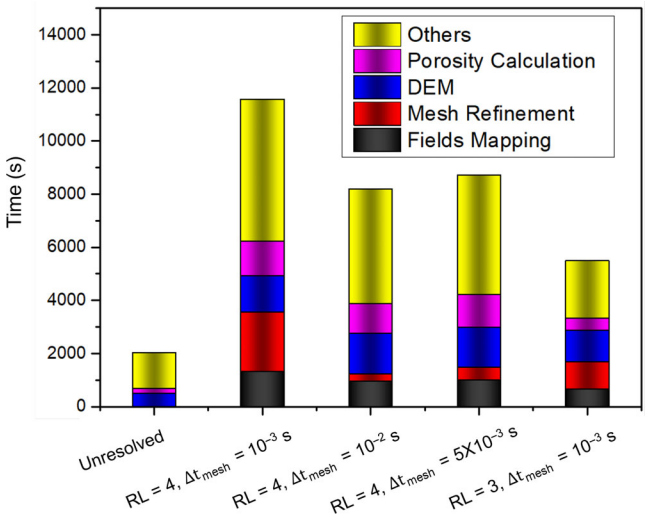


**FIGURE 17** Breakdown of time consumption in various simulation procedures for the spouted bed case.

10% of that in the resolved method. Accordingly, the semi-resolved solver roughly reduces the computational cost to lower than one-tenth of the resolved solver. The increase in computational efficiency is mainly due to the flexible algorithm for the particle resolution as well as the dynamic mesh refinement, which significantly reduces the number of CFD mesh cells.

On the other hand, the simulation case of the spouted bed provides a direct comparison between the semi- and the un-resolved CFD-DEM. The distribution of time allocation across various simulation procedures is presented in Figure 17. The time allocation encompasses subroutines involving DEM calculations, CFD computations for mesh refinement, field mapping, porosity calculations, and others. To provide a basis for comparison, we also conducted unresolved CFD-DEM simulations that excluded coarse particles. As depicted in Figure 17, the unresolved simulations exhibit the lowest computational cost, while the RL = 4 and $\Delta t_{mesh} = 10^{-3}$ configuration records the highest computational time, approximately six times longer than the unresolved case. However, the computational expense can be significantly mitigated either by extending the remeshing interval ($RL = 4$, $\Delta t_{mesh} = 10^{-2}$) or by reducing the mesh refinement level ($RL = 3$, $\Delta t_{mesh} = 10^{-3}$). As Figure 16 highlighted, when the remeshing interval is set at a high value, mesh refinement encounters challenges in rapidly capturing the motion of high-speed particles. Consequently, this approach is not recommended. Furthermore, the total computation time appears to be more responsive to changes in mesh refinement levels than to adjustments in the remeshing interval, indicating that exploring an appropriate mesh refinement level is a more suitable strategy for achieving enhanced computational efficiency.

When comparing with existing semi-resolved CFD-DEM methods, our method incorporates a porosity model allowing for a more precise representation of solid volumes within the CFD meshes. Consequently, this leads to enhanced simulation accuracy in both the fluid field and fluid-particle interaction forces. Moreover, previous semi-resolved methods predominantly employed uniform refined meshes across the entire computational domain, inevitably resulting in computational costs approaching those of resolved methods. In contrast, our current approach utilizes dynamic mesh refinement, focusing on refining the mesh near the boundaries of the coarse particle, which substantially reduces the total mesh number. The disadvantage of this approach lies in the necessity of incorporating a field mapping procedure into the calculations, which incurs some time overhead. Therefore, the computational efficiency of the proposed semi-resolved method should be subject to a detailed evaluation in the future when other methods become accessible.

## 7 | CONCLUSION

A two-grid semi-resolved CFD-DEM approach has been proposed, which is suitable for particle-fluid flow scenarios with a high particle size ratio, such as bi-modal particle systems. The semi-resolved CFD-DEM method provides a trade-off between computational efficiency and accuracy, with its range of applicability falling somewhere between resolved and unresolved solvers.

1. Using two CFD grids is an effective solution to address the challenge of balancing the requirements of resolving the fluid flow in the pore space and maintaining a realistic porosity field for the fine particles. This approach is easy to implement and provides great flexibility. Additionally, it has been found that a solid volume compensation procedure can ensure total solid volume conservation in the system.
2. In the case of bi-modal distributed particle systems, which is the main application scenario of this semi-resolved solver, it was found that while the proposed solver provided a highly accurate estimation of the fluid-particle interaction force for the coarse particles, the accuracy of the force prediction for each individual fine particle was relatively low. This was due to the limitations of the empirical drag models and this is a fundamental issue with any unresolved approach to CFD-DEM coupling. However, the accuracy can still be improved by applying the empirical model which performs best for the particular range of volume fraction of fine particles in the system.
3. While the computational cost of the semi-resolved CFD-DEM method depends on various factors such as the volume fraction of coarse particles and the size of the computational domain, our simulations have demonstrated that for a typical scenario involving a particle assembly with a size ratio of 4, the use of two sets of CFD grids can lead to a reduction of the total computational cost by about one order of magnitude.

### AUTHOR CONTRIBUTIONS

**Hanqiao Che:** conceptualization (equal); formal analysis (equal); investigation (equal); methodology (equal); software (equal); visualization (equal); writing – original draft (equal). **Kit Windows-Yule:** supervision (equal); writing – review and editing (equal). **Catherine O'Sullivan:**

conceptualization (equal); writing – review and editing (equal). **Jonathan Seville:** writing – review and editing (equal).


## ACKNOWLEDGMENTS

This work was supported by EPSRC New Investigator Award EP/T034327/1 and EPSRC EP/P010393/1.


## DATA AVAILABILITY STATEMENT

The numerical data from Figures 6, 7 and 9–14 have been tabulated in the Appendix S1. The source code of the resolved CFD-DEM solver, *cfdemSolverIBPICI*, along with the verification cases, is provided as a .zip file in the Appendix S2. Additionally, the source code is available as open-source on Github at https://github.com/uob-positron-imaging-centre/PICI-CFDEM-IB. To compile *cfdemSolverIB-PICI*, it should be used in conjunction with OpenFOAM-5.x, which can be found at https://github.com/OpenFOAM/OpenFOAM-5.x.

## NOMENCLATURE: GREEK SYMBOLS

| | |
|---|---|
| $\omega$ | angular velocity (rad/s) |
| $\mu$ | dynamic Viscosity (Pa·s) |
| $\psi$ | correction factor of fluid velocity($m^2/s$) |
| $\rho$ | density ($kg/m^3$) |
| 1. | $\varepsilon$] porosity (-) |
| $\phi$ | solid volume fraction (-) |
| $\boldsymbol{\tau}$ | viscous force tensor (Pa) |

## 8 | LATIN SYMBOLS

| | |
|---|---|
| $D$ | diameter of the largest particle (m) |
| $d$ | diameter (m) |
| $e$ | coefficient of restitution (-) |
| $\mathbf{F}$ | force (N) |
| $G$ | momentum source coefficient ($N/m^3$) |
| $\mathbf{g}$ | gravitational acceleration ($m/s^2$) |
| $\mathbf{I}$ | inertia of rotation ($kg\ m^2$) |
| $M$ | torque (N m) |
| $m$ | mass (kg) |
| $N$ | particle number (-) |
| $p$ | pressure (Pa) |
| PC | Pearson correlation coefficient (-) |
| $R$ | radius (m) |
| RL | refinement level (-) |
| $\mathbf{S}$ | source term ($m/s^2$) |
| $s$ | tangential overlap (m) |
| $t$ | time (s) |
| $\mathbf{u}$ | velocity (m/s) |
| $V$ | volume ($m^3$) |
| $W$ | weight (-) |

## SUB/SUPERSCRIPTS

| | |
|---|---|
| cell | CFD mesh cell |
| coarse | coarse particle |
| $f$ | fluid |
| fine | fine particle |
| $l$ | local |
| $p$ | particle |
| pf | particle-fluid |
| $pp$ | particle-particle |
| prev | previous time step |
| $r$ | radical |
| reso | resolved |
| $s$ | solid |
| Stokes | Stokes force |
| total | total number |
| unreso | unresolved |


## ORCID

*Hanqiao Che* https://orcid.org/0000-0002-7479-3504
*Kit Windows-Yule* https://orcid.org/0000-0003-1305-537X
*Jonathan Seville* https://orcid.org/0000-0003-0207-3521


## REFERENCES


1. Knight PC. Structuring agglomerated products for improved performance. *Powder Technol*. 2001;119:14-25.
2. Jens U, Raquel C, Jean-Claude C. Product design and engineering — past, present, future trends in teaching, research and practices: academic and industry points of view. *Curr Opin Chem Eng*. 2020;27:10-21.
3. Skempton AW, Brogan JM. Experiments on piping in sandy gravels. *Geotechnique*. 1994;44:449-460.
4. Kenichi K. Numerical evaluation of internal erosion due to seepage flow. Imperial College London Thesis. 2016.
5. Zhou ZY, Kuang SB, Chu KW, Yu AB. Discrete particle simulation of particle–fluid flow: model formulations and their applicability. *J Fluid Mech*. 2010;661:482-510.
6. Zhu HP, Zhou ZY, Yang RY, Yu AB. Discrete particle simulation of particulate systems: theoretical developments. *Chem Eng Sci*. 2007;62:3378-3396.
7. Luo K, Wang Z, Fan J, Cen K. Full-scale solutions to particle-laden flows: Multidirect forcing and immersed boundary method. *Phys Rev E*. 2007;76:066709.
8. Hazmil AAM, Fabien E, Berend W. An immersed boundary method for incompressible flows in complex domains. *J Comput Phys*. 2019;378:770-795.
9. Zhang C, Wu C, Nandakumar K. Effective geometric algorithms for immersed boundary method using signed distance field. *J Fluids Eng*. 2019;141:061401.
10. Alice H. *CFD-DEM on Multiple Scales - an Extensive Investigation of Particle-Fluid Interactions*. Thesis. 2014.
11. Boyce CM, Holland DJ, Scott SA, Dennis JS. Novel fluid grid and voidage calculation techniques for a discrete element model of a 3D cylindrical fluidized bed. *Comput Chem Eng*. 2014;65:18-27.
12. Clarke DA, Sederman AJ, Gladden LF, Holland DJ. Investigation of void fraction schemes for use with CFD-DEM simulations of fluidized beds. *Ind Eng Chem Res*. 2018;57:3002-3013.
13. Feng YQ, Yu AB. Effect of bed thickness on the segregation behavior of particle mixtures in a gas fluidized bed. *Ind Eng Chem Res*. 2010;49:3459-3468.
14. Wang S, Huilin L, Li X, Wang J, Zhao Y, Ding Y. Discrete particle simulations for flow of binary particle mixture in a bubbling fluidized bed with a transport energy weighted averaging scheme. *Chem Eng Sci*. 2009;64:1707-1718.

15. Beetstra R, Van der Hoef MA, Kuipers HAM. Numerical study of segregation using a new drag force correlation for polydisperse systems derived from lattice-Boltzmann simulations. *Chem Eng Sci*. 2007;62:246-255.
16. Christopher K. *Fluid Flow and Drag in Polydisperse Granular Materials Subject to Laminar Seepage Flow*. Thesis. 2018.
17. Takuya T, Kyohei H, Yoshitomo O, Toshitsugu T. Fictitious particle method: a numerical model for flows including dense solids with large size difference. *AIChE J*. 2014;60:1606-1620.
18. Kuang C, Yin W, Qing Y. A semi-resolved CFD-DEM model for seepage-induced fine particle migration in gap-graded soils. *Comput Geotech*. 2018;100:30-51.
19. Qing Y, Kuang C, Yin W, Mahmood A. Improvement of semi-resolved CFD-DEM model for seepage-induced fine-particle migration: eliminate limitation on mesh refinement. *Comput Geotech*. 2019;110:1-18.
20. Zekun W, Yujun T, Moubin L. A semi-resolved CFD–DEM approach for particulate flows with kernel based approximation and Hilbert curve based searching strategy. *J Comput Phys*. 2019;384:151-169.
21. Zekun W, Moubin L. On the determination of grid size/smoothing distance in un/semi-resolved CFD-DEM simulation of particulate flows. *Powder Technol*. 2021;394:73-82.
22. Zhouzun X, Shuai W, Yansong S. A novel hybrid CFD-DEM method for high-fidelity multi-resolution modelling of cross-scale particulate flow. *Chem Eng J*. 2023;455:140731.
23. Jun C, Jingxin Z. A semi-resolved CFD-DEM coupling model using a two-way domain expansion method. *J Comput Phys*. 2022;469:111532.
24. Rui S, Heng X. Diffusion-based coarse graining in hybrid continuum–discrete solvers: theoretical formulation and a priori tests. *Int J Multiphase Flow*. 2015;77:142-157.
25. Chih-Chia H, Oijen JA, Deen NG, Yali T. A particle-size dependent smoothing scheme for polydisperse Euler-Lagrange simulations. *Chem Eng Sci*. 2023;277:118765.
26. Jesse C, Olivier D, Fox Rodney O. On fluid–particle dynamics in fully developed cluster-induced turbulence. *J Fluid Mech*. 2015;780:578-635.
27. Jesse C, Olivier D, Fox Rodney O. Strongly coupled fluid-particle flows in vertical channels. I. Reynolds-averaged two-phase turbulence statistics. *Phys Fluids*. 2016;28:033306.
28. Surya D, Tafti DK. A novel two-grid formulation for fluid–particle systems using the discrete element method. *Powder Technol*. 2013;246:601-616.
29. Kazuya T, Mikio S. Flexible discretization technique for DEM-CFD simulations including thin walls. *Adv Powder Technol*. 2020;31:1825-1837.
30. Roland G, Tsorng-Whay P, Hesla Todd I, Joseph Daniel D, Jacques P. A fictitious domain method with distributed Lagrange multipliers for the numerical simulation of particulate flow. *Contemp Math*. 1998;218:121-137.
31. Glowinski R, Pan TW, Hesla TI, Joseph DD. A distributed Lagrange multiplier/fictitious domain method for particulate flows. *Int J Multiphase Flow*. 1999;25:755-794.
32. Christoph K, Christoph G, Alice H, Stefan A, Stefan P. Models, algorithms and validation for opensource DEM and CFD-DEM. *Progr Comput Fluid Dyn*. 2012;12:140-152.
33. Barbara B, Thomas B, Laurent L, Olivier T. A simple immersed-boundary method for solid–fluid interaction in constant- and stratified-density flows. *Comput Fluids*. 2014;97:126-142.
34. Anderson TB, Roy J. Fluid mechanical description of fluidized beds. Equations of motion. *Ind Eng Chem Fundamentals*. 1967;6:527-539.
35. Muhammed F, Lambert O. *Handbook of Powder Science & Technology*. Springer Science & Business Media; 2013.
36. Tsuji Y, Tanaka T, Ishida T. Lagrangian numerical simulation of plug flow of cohesionless particles in a horizontal pipe. *Powder Technol*. 1992;71:239-250.
37. Zhang HP, Makse HA. Jamming transition in emulsions and granular materials. *Phys Rev E*. 2005;72:011301.
38. Kempe T, Schwarz S, Fröhlich J. Modelling of spheroidal particles in viscous flows. Paper presented at: Proceedings of the Academy Colloquium Immersed Boundary Methods: Current Status and Future Research Directions; KNAW, 15–17 June. 2009; Amsterdam, The Netherlands:845 1994.
39. Jing L, Kwok CY, Leung YF, Sobral YD. Extended CFD–DEM for free-surface flow with multi-size granules. *Int J Num Anal Methods Geomech*. 2016;40:62-79.
40. Link JM, Cuypers LA, Deen NG, Kuipers JAM. Flow regimes in a spout–fluid bed: a combined experimental and simulation study. *Chem Eng Sci*. 2005;60:3425-3442.
41. Shirgaonkar Anup A, MacIver Malcolm A, Patankar NA. A new mathematical formulation and fast algorithm for fully resolved simulation of self-propulsion. *J Comput Phys*. 2009;228:2366-2390.
42. Weller HG, Tabor G, Jasak H, Fureby C. A tensorial approach to computational continuum mechanics using object-oriented techniques. *Comput Phys*. 1998;12:620-631.
43. Chris K, Catherine O'S, Berend W, Daniele D. Computing drag and interactions between fluid and polydisperse particles in saturated granular materials. *Comput Geotech*. 2020;117:103210.
44. Thornton C. Numerical simulations of deviatoric shear deformation of granular media. *Géotechnique*. 2000;50:43-53.
45. Fabian D, Wachem BGM. Fully-coupled balanced-force VOF framework for arbitrary meshes with least-squares curvature evaluation from volume fractions. *Num Heat Transf Pt B Fundamentals*. 2014;65:218-255.
46. Hanqiao C, Catherine O'S, Adnan S, Smith Edward R. A novel CFD-DEM coarse-graining method based on the Voronoi tessellation. *Powder Technol*. 2021;384:479-493.
47. Zick AA, Homsy GM. Stokes flow through periodic arrays of spheres. *J Fluid Mech*. 1982;115:13-26.
48. Abbas ZA, Takuya T, Toshitsugu T. A new relation of drag force for high stokes number monodisperse spheres by direct numerical simulation. *Adv Powder Technol*. 2014;25:1860-1871.
49. Hill RJ, Koch DL, Ladd AJ. The first effects of fluid inertia on flows in ordered and random arrays of spheres. *J Fluid Mech*. 2001;448:213-241.
50. Tenneti S, Garg R, Subramaniam S. Drag law for monodisperse gas–solid systems using particle-resolved direct numerical simulation of flow past fixed assemblies of spheres. *Int J Multiphase Flow*. 2011;37:1072-1092.
51. Ergun S. Fluid flow through packed columns. *Ind Eng Chem*. 1952;48:89-94.
52. Di Felice R. The voidage function for fluid-particle interaction systems. *Int J Multiphase Flow*. 1994;20:153-159.
53. Tang Y, Peters EAJF, Kuipers JAM, Kriebitzsch SHL, Hoef MA. A new drag correlation from fully resolved simulations of flow past monodisperse static arrays of spheres. *AIChE J*. 2015;61:688-698.

## SUPPORTING INFORMATION

Additional supporting information can be found online in the Supporting Information section at the end of this article.

**How to cite this article:** Che H, Windows-Yule K, O'Sullivan C, Seville J. A novel semi-resolved CFD-DEM method with two-grid mapping: Methodology and verification. *AIChE J*. 2023; e18321. doi:10.1002/aic.18321